Context-Aware Mesh Smoothing for Biomedical Applications

Tobias Moench[a,*], Rocco Gasteiger[a], Gabor Janiga[b], Holger Theisel[a], Bernhard Preim[a]

[a]*Department of Simulation and Graphics, University of Magdeburg, Germany*
[b]*Institute of Fluid Dynamics and Thermodynamics, University of Magdeburg, Germany*

Abstract

Smoothing algorithms allow to reduce artifacts from mesh generation, but often degrade accuracy. Thus, we present a method that identifies staircase artifacts which result from image inhomogeneities and binary segmentation in medical image data for subsequent removal by adaptive mesh smoothing. This paper makes the following specific contributions: caps, which are flat regions, resulting from segmentation or clipping at the endings of anatomical structures are detected and modified by smoothing; the effects of the adaptive smoothing method involving context information are quantitatively analyzed with respect to accuracy and their influence on blood flow simulations; the image stack orientation, which is relevant for this context-aware smoothing approach, is estimated automatically from the surface models. Thus, context-aware smoothing enables to adaptively smooth artifact areas, while non-artifact features can be preserved. The approach has been applied to CT neck datasets, as well as phantom data and the results are evaluated regarding smoothness and model accuracy. The accuracy of model orientation estimation and cap detection has been evaluated for clinical and phantom data. Finally, context-aware smoothing has been applied to CT angiography data for the simulation of blood flow. The simulation results are presented and prove the general suitability of context-aware smoothing.

Keywords: Mesh smoothing, model generation, surgical planning, simulation, CFD

1. Introduction

The morphology of anatomic and pathologic structures and their spatial relations are examined for planning of surgical intervention or radiation treatment. Surface models of anatomical structures are usually derived from tomographic medical image data (e.g., from computed tomography (CT) or magnetic resonance imaging (MRI)). Tomographic image data often suffer from a limited resolution and exhibit anisotropic voxels (slice distance is considerably larger than the in-plane resolution). Although, low slice distances and an isotropic resolution is technically feasible with the latest generation CT scanners, clinical data still often exhibit a large anisotropy. This may be due to the devices, e.g., older CT or MRI scanners, due to the goal to minimize ionizing radiation, or simply to recude the amount of data which often significantly affects waiting times because of low-bandwidth networks. For generating surface meshes, the target structures need to be identified and delineated by user interaction, automatic or semi-automatic segmentation methods. In simple cases, e.g., when air-filled structures in CT data should be displayed, the surface can be extracted directly from the intensity data. Often, this is not feasible since tomographic image data, acquired in clinical routine, may suffer from inhomogeneities or similar intensity values of neighboring structures complicating their segmentation. Applying the segmentation information to the intensity data, e.g., by masking, such problems can be overcome. 3D models, generated from intensity data and such segmentation information, may contain several artifacts, such as staircases, terraces, holes, and noise. For a correct and convenient perception of shapes and spatial relations, the models should look naturally to resemble, e.g., the intraoperative experience of surgeons. The natural appearance refers to smoothness of the surface, since anatomical structures usually do not exhibit sharp edges. Feature edges attract the observers' attention and might severely disturb perception of the overall shape and structure of the surface model. Artifacts can be reduced during mesh generation or by additional mesh post-processing (smoothing). Unfortunately, features, which are not caused by model generation, might get removed and the structures' volume, extent, and relevant inter-structure distances may get altered. Mesh smoothing methods, in general, apply a uniform filter to the surface mesh. Artifacts, however, are often not uniformly spread over the surface (see Fig. 1(a)). As a result of uniform surface smoothing, artifacts get reduced, but as a side-effect non-artifact areas might get altered too much (see Fig. 1(b)). As a remedy, feature-sensitive smoothing was suggested [1], which detects features and adjusts the sampling accordingly to reduce modifications of these features. This and other related methods (e.g., [2, 3, 4]) are successful in preserving sharp edges, such as in CAD models or laser scanning data. The artifacts in tomographic medical image data may result from anisotropic voxels and from involving (binary) segmentation information in the model generation process. Since features are not discriminated with respect to their origin, staircase artifacts would be maintained by such feature-preserving smoothing methods. Context information, such as slice orientation, slice distance and knowledge on the properties of artifacts

*Corresponding author
Email address: tobias.moench@ovgu.de (Tobias Moench)

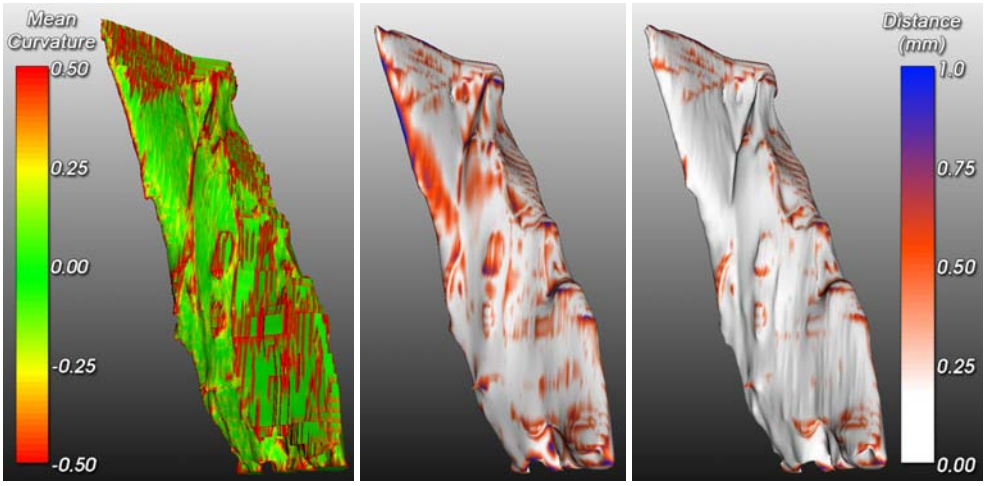

(a) Original Model (b) Uniform Laplacian Smoothing (c) Context-aware Laplacian Smoothing

Figure 1: Context-aware smoothing applied to a surface model of the sternocleidmastoid muscle. (a) The initial model generated via the marching cubes algorithm, colored by mean curvature; (b) Uniform Laplacian filtering; (c) Context-aware Laplacian filtering. (b) and (c) are colored by the minimum Euclidean distance (of each vertex) to the surface of the original model shown in (a).

are usually not considered for a locally adaptive artifact reduction.

To account for the described problems, we present an extended approach for the detection of staircase artifact areas, which has partly been described in [5]. Determining the distance to these identified artifacts, we can apply weights to the displacement vectors of each vertex during the smoothing procedure. Thus, our approach can be integrated into any available mesh smoothing method. As a result, only the artifact areas of the surface are smoothed adaptively (see Fig. 1(c)) in contrast to uniform Laplacian smoothing (see Fig. 1(b)), where the surface is modified in artifact and non-artifact areas. This allows to preserve model accuracy in non-artifact areas which is important in 3D diagnostic or surgical planning applications. We refer to this concept as *context-aware* smoothing.

For the simulation of blood flow, flow inlets and outlets are defined by clipping the vessel branches perpendicular to the centerline. The resulting flat areas (caps), which may be oriented arbitrarily with respect to the image stack orientation, would get distorted during further mesh processing (e.g., smoothing). Thus, manual clipping is usually the last step in surface model generation pipeline used as input for the generation of a volume mesh for computational fluid dynamics (CFD) simulations. The detection and preservation of arbitrarily oriented caps would thus yield more flexibility for related workflows, since additional smoothing steps could easily and automatically be carried out after defining the in- and outlets.

Besides CFD, the segmentation of image data usually focusses on a defined region of interest, which often contains only a part of the structure. Especially elongated structures, such as vessels and muscles, are cut during the segmentation process resulting in flat, clipped areas. Caps, whose flat regions are oriented according to the image stack orientation (e.g., z-axis), might get detected as staircase areas and subsequently be smoothed. Furthermore, caps with a surface normal differing strongly from the image stack orientation might not get smoothed. In contrast to CFD, medical visualization might also require rounded caps to prevent abrupt endings [6]. A correct and consistent handling of these endings requires their identification. This allows to preserve the caps for measurement tasks or to consistently generate smooth endings for visualization. Context-aware smoothing implies knowledge on the image stack orientation (usually the z-axis) as basic information for the differentiation of staircase artifacts. If the coordinate system of the target structure is modified, e.g., the surface model is being aligned with another reference structure, context-aware smoothing could not be applied due to the missing correlation between the staircase artifact orientation and the original image stack orientation. In such a case, the orientation information needs to be recovered.

Surface models of anatomical structures are widely used for planning of surgical interventions, e.g., for ablations of the liver [7] or tumor resections [8], where the exact location of the tumor, metastases or vascular structures [9, 10, 11] needs to be known to provide a high degree of safety for the patient. Similarly, high accuracy during model generation is also required in orthopedics, e.g., for osteotomy planning [12], or for neck surgery. Here, several critical structures (e.g., arteria carotis, vena jugularis, sternocleidomastoid muscle, lymph nodes, salivary glands) are located very close to each other, which makes accurate surface models a basic requirement for, e.g., measurement tasks during planning of surgical interventions or further treatment [13]. High model accuracy *and* surface smoothness is also relevant for biophysical and biomechanical simulations, e.g., of blood flow in order to estimate the rupturing risk of an aneurysm. Thus, we applied context-aware smoothing to sample data acquired for surgery planning and blood flow simulation. We investigated the influence on smoothness, distance and volume preservation.

2. Related Work

Suface models of anatomical structures are generated from raw medical image data or binary masks that are derived from volume data by preprocessing and segmenting the target structures (e.g., bones, vessels, liver, lymph nodes). Additional filtering, such as smoothing, erosion, dilation, of the intensity data or segmentation masks can reduce discontinuities in the resulting surface, but may remove features or change relevant properties of the structure [14]. The work of Neubauer et al. [15] provides an example for such an image processing pipeline for the reduction of staircase artifacts by combining, e.g., erosion, dilation and distance metrics. The anisotropy problem can be overcome, e.g., by shape-based interpolation [16]. Interpolating intermediate slices results in much more data and computational effort. In clinical routine, this additional effort is often prohibitive, since data with lower resolution is usually acquired deliberately to save time and storage. Furthermore, large staircases from anisotropic, segmented image data may not get removed sufficiently since the interpolation treats the staircases locally, whereas their effect is more global. The data can be transformed into a surface mesh using, e.g., the Marching Cubes (MC) algorithm [17], or level-set methods [18]. Several methods take care of artifacts during mesh generation, e.g., by additional trilinear interpolation and subdivision of the surface elements (Precise MC [19]), by detecting features and adjusting the data sampling accordingly [1], or by iterative constrained relaxation of the surface (e.g., Dual MC [20], Constrained Elastic Surface Nets (CESN) [21, 22]). Some of the methods, such as Precise MC, achieve better visual quality at the expense of a significant loss of performance. The reduction of strong artifacts, such as staircases, goes along with a loss of smaller, potentially relevant details and large terraces may still remain. The original CESN approach [21] extracts the initial surface from binary image data and restricts the movement of each single vertex to the initial voxel cells. Additionally involving intensity information during the relaxation procedure allows for higher accuracy [22]. Large staircase artifacts, e.g., from anisotropic image data, may still not be reduced sufficiently and relevant features might get removed. The extended MC [1] accounts for aliasing artifacts degrading surface features edges. As a result, features are better reproduced during model generation. Unfortunately, both, relevant geometric details and staircase artifacts, would be maintained.

Similarly, noise, staircase artifacts, or plateaus resulting from the limited resolution can be reduced after mesh generation by appropriate smoothing operations (e.g., Laplace filter, Mean Curvature Flow (Laplace with cotangential weights) [2]). These methods allow to smooth surface models but cause volume shrinkage and loss of features. More specialized methods (Laplace+HC [3], Taubin's $\lambda|\mu$ smoothing [23]) try to prevent from shrinking volumes by an additional correction step or by restricting the vertex movement according to surface confidence values [24]. The Laplace+HC algorithm [3] introduces further parameters to control the influence of the initial vertex position and the displacement of the neighboring vertices. Similarly, Taubin's $\lambda|\mu$ filter [23], improves the default, Laplacian smoothing by adding a second, negatively weighted Laplacian filter step, which considers the displacement of the neighboring vertices and accounts for volume shrinkage. For models containing extreme staircase artifacts (e.g., Figs. 1(a) and 4), an appropriate parameter configuration is hard to find, if a natural appearance and accuracy are required simultaneously. Surfaces, generated from laser scanning data, often exhibit noise which can be removed using various mesh smoothing methods (e.g., [4, 25, 26]). These methods focus on the preservation of sharp edges in non-medical data [27, 28, 29]. Their direct application to medical surface models likely yields unsatisfying results, since anatomical structures typically exhibit smoother shapes. Belyaev and Ohtake [30] compared different mesh smoothing methods, but did not consider different requirements of anatomical structures. In contrast, Bade et al. [31] applied different smoothing algorithms to anatomical surface models generated from binary image data and compared the results with respect to artifact reduction and volume preservation. They identified the Laplace+HC and Taubin's $\lambda|\mu$ smoothing as most appropriate for most anatomical structures with respect to volume and feature preservation. Additionally, they suggested a constraint for vertex placement during mesh filtering to preserve accuracy [32], which is similar to the CESN approach [21]. These smoothing algorithms are suitable for the reduction of small artifacts (staircases, noise) with simultaneous preservation of accuracy. Large staircase artifacts can still not be sufficiently reduced whilst accuracy is required.

All of these widely used methods apply constant smoothing parameters to the target structure. In contrast, there exist other methods that adjust smoothing according to classified features [33, 34], local mesh density [35], or even apply different filters [36] to preserve detected features. Thus, most feature-sensitive methods would maintain the artifacts in medical surface models. Furthermore, there is no mesh smoothing method available, which focuses smoothing to artifact areas and thus tries to split up the smoothing process for different problems.

Besides smoothing, other mesh processing techniques also have impact on the smoothness. Generating high resolution meshes from resampled image data and subsequently decimating it using, e.g., quadric error metrics [37] or the progressive meshes approach [38], reduces several (small) surface artifacts with controlled error. Decimation methods are, unfortunately, not designed for artifact removal, but to maintain relevant features possibly resulting in a preservation of dominant features, such as staircases.

Accurate and smooth surface meshes are used as input for volume mesh generation in biomedical CFD, e.g., for the patient-specific simulation of blood flow in vascular systems [39, 40]. Usually, the model generation pipeline involves different steps for segmenting the target structures and preparing them for simulation [41]. Thereby, a surface mesh approximating the underlying anatomical vessel morphology faithfully is necessary for the volume grid generation. Depending on the involved methods (segmentation and surface reconstruction), the resulting surfaces can be very different

yielding to varying simulation results for the same structure [42]. Since the extraction of surfaces for usage in CFD can be complex and time consuming if manual correction of artifacts and inhomogeneities is involved, a more automated procedure is desirable. The use of MPU Implicits [43] based on points clouds from binary segmentation masks seems promising, but ignores the intensity information of the image data. The latter allows for higher accuracy, but might introduce topologically wrong models due to image inhomogeneities leading, e.g., to merged vessels.

3. Methods

Our adaptive smoothing procedure consists of three steps:
(I) an initial identification of the artifacts,
(II) a computation of weights for smoothing, and
(III) the application to the smoothing algorithm.

These steps have been presented in [5] in full detail. We extended the approach of staircase-aware smoothing to allow for an estimation of the image stack orientation (see Sec. 3.1) and an algorithm for the detection and preservation of caps (see Sec. 3.3). The algorithm for staircase detection and weighting is, however, partly described in Section 3.2, since several details are required for understanding of the further extensions and results.

As prerequisites for context-aware smoothing, we assume that all surface normals are consistently pointing either towards the outside or the inside of the model and the normals of neighboring faces do not suddenly point to the opposite side. As a result, we can assume that faces being perfectly orthogonal to the image stack orientation (typically along z-axis) have normals parallel to it and vice versa. This orientation information can be derived directly from the image data since it is usually represented in the header information. If the image stack orientation is not known, e.g., because smoothing is not applied within the surface reconstruction process, or the surface model's orientation has been modified for registration/alignment reasons, it needs to be recovered. Thus, we present an additional, but optional, step, which enables the estimation of the image stack orientation from the surface model.

Staircases can be characterized as perpendicular surface areas. This information is usually not sufficient to reliably detect staircase artifacts for two reasons:

- Other (relevant) features with similar feature angles might be contained in the model which should not receive a high weighting for the smoothing algorithm.
- Depending on the initially applied mesh generation algorithm, these staircase "borders" might have been smoothed already slightly. Thus, the features within the staircases would exhibit similar curvature values as other "natural" features.

As a result, we employ knowledge on the (estimated) image stack orientation, slice distance and on relative changes between faces in and orthogonal to the image stack orientation. Especially for data with strongly anisotropic voxel dimensions, the dihedral angles at the feature edges tend to get closer to 90 degree. For nearly isotropic voxels, these angles might get smaller. Thus, our approach allows to interactively adjust its sensitivity for different sizes of staircase artifacts. After computing the initial orientation rating, the vertices, belonging to staircase artifacts, are weighted to allow for subsequent usage during mesh smoothing. This is described in detail in the following subsections.

3.1. Estimation of the Image Stack Orientation

The identification of staircases requires knowledge on the image stack orientation of the source image data. For the estimation of the image stack orientation, we assume that the model contains several staircase artifacts. It is not necessary, that the exact location of the artifacts is known. The presence of staircase artifacts, however, allows to detect and extract clusters of similar face normals and approximate the overall model orientation. Within this section, we will refer to the term "normals" also as "samples" since we treat the normal vectors as points on a unit sphere (see Fig. 2).

To identify these clusters, we extract all face normals and regard them as samples in 3D space, where similar normals form clusters. For example, for a spherical surface model, the normals would result in a uniformly sampled Gauss map.

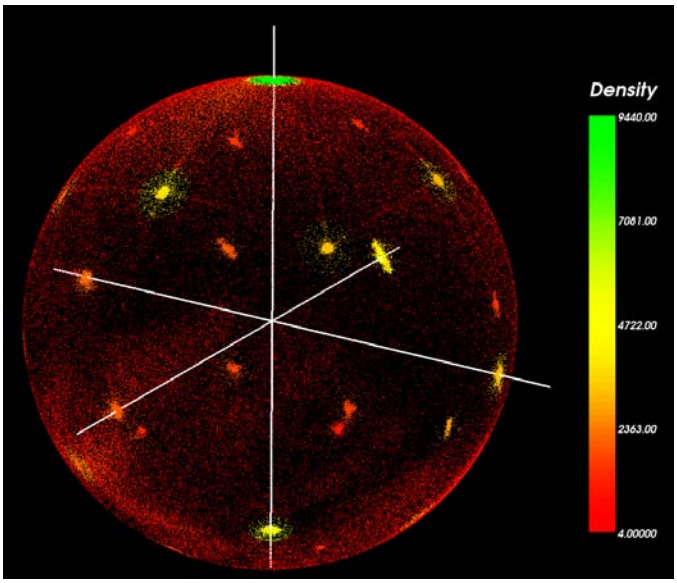

Figure 2: Gauss map of the face normals of a liver model. Regions with higher density are clearly visible (colored yellow/green). Density is shown according to the number of samples within the radius r.

As a next step, we compute the density of the samples by counting the number of samples within a given radius r (default value is 0.1). Thus, iterating over all samples yields one density value per sample which can then be used to apply a density threshold to the whole point cloud (see Fig. 2). This threshold allows to remove samples which do not belong to one of the dominant clusters. The value is automatically adjusted according to the average of the mean and maximum density value. This value

has turned out to be sufficient among all tested datasets. After reducing the point cloud to the high density clusters, we label all samples according to their Euclidean distance to other labeled samples. For that, we start with a random sample and iteratively consider all samples within the defined range r as further candidates. After labeling the current sample, we proceed with the identified candidate samples. If no new samples for the current cluster are found, we proceed with the remaining unlabeled samples in the same way. This region-growing-like clustering method does not require a predefined number of clusters or further parameters. Computing the center of each labeled point cloud region representing clustered face normals, we obtain the average, that is regarded as potential image stack orientation vector.

To determine the vector with highest probability of describing the image stack orientation, we compute the relative orientation θ_{f_i} of all faces f_i with respect to each potential orientation vector. The relative face orientation is defined as the dot product of the face normal and a given orientation vector. The resulting values are scaled to the range of [0,1] according to Eq. 1. Thus, for faces with normals being orthogonal to the orientation vector the relative orientation θ_{f_i} equals 1, whereas for faces with normals being parallel to slice orientation it equals 0.

$$\forall f_i \in F: \quad \theta_{f_i} = 1 - \left|\vec{n}_{f_i} \cdot \vec{n}_{stack}\right| \tag{1}$$

$\vec{n}_{f_i}, \vec{n}_{stack}$ - normal vector of f_i and image stack orientation

$f_i \in F$; F - set of faces of mesh M

$\theta \in [0, 1]$; θ_{f_i} - orientation of face f_i

This computation is performed for each potential orientation vector, whereby we search for the vector maximizing the number of faces being almost orthogonal to this orientation vector. Hence, we count all faces, where θ_{f_i} is less then 0.05 which equals a tolerated deviation angle of 4.5 degree. This value has also been chosen empirically. The results are quite robust with respect to this parameter. Higher values, e.g., 0.1, which equals 9 degree deviation, gave almost similar results. Finally, the vector maximizing the number of orthogonal faces is chosen as image stack orientation.

The described method for the estimation of the image stack orientation to re-establish the correlation between the surface model and the orientation of slices in the image data obviously depends on the existence of staircase artifacts. The correct vector can only be detected if the number of faces belonging to staircases exceeds a certain level, depending on the size and resolution of the model. Thus, if there are just very small staircases present in the model, the estimation process will return a vector which cannot correctly describe the image stack orientation. This fact will be examined further in the results section.

3.2. Context-Aware Smoothing

The procedure for the identification and weighting of staircases has already been presented in [5]. The definition of

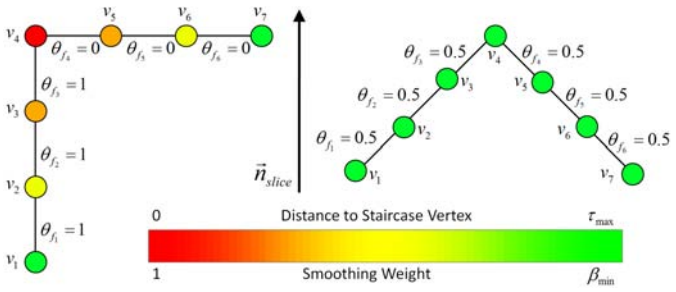

Figure 3: 2D illustration of a staircase (left) and a similar feature (right) that is not related to the image stack orientation ($\vec{n}_{stack}$).

weights for the vertices of a surface mesh allows to smooth only artifact areas (with high weights), whereas areas without artifacts (with low weights) remain unchanged. For completeness and better understanding of the extensions and further applications, we are going to explain this process briefly in the following sections.

3.2.1. Identification of Staircase Artifacts

At first, it is necessary to determine the relative orientation θ_{f_i} of each single face f_i (see Figs. 4(a) and 3) with respect to the image stack orientation. The orientation may have been estimated earlier (see Section 3.1). Otherwise, a manually specified vector (usually the vector is set along the z-axis (0,0,1)) is employed for further computation. The relative face orientation is then determined as described in the previous subsection (see Eq. 1).

As a next step, the orientation change θ'_{v_j} at each vertex v_j is computed as the difference between the maximum and the minimum face orientation of all incident faces F_{v_j} at that vertex. Thus, for vertices at perfect staircase edges, where the maximum difference of the incident faces would equal 90 degree, θ'_{v_j} would equal 1. For flat areas, θ'_{v_j} equals 0. The orientation change yields visually similar results as typical curvature measures (see Fig. 4(b)) as it highlights feature edges, but is related to the image stack orientation. Thus, features, which are related to the image stack orientation, get highlighted, whereas non-artifact features, which are not caused by segmentation and a large slice distance, receive a lower weighting (compare Fig. 3 left and right).

3.2.2. Artifact Weighting

In the previous step, all vertices have been weighted according to changes of the relative orientation which depends on the image stack orientation. To enable adaptive smoothing of the staircases, we define weights for all vertices belonging to the artifact areas. Thus, we apply a threshold $\tau_{\theta'}$ and extract only the vertices with $\theta'_{v_j} > \tau_{\theta'}$. We have empirically determined to set $\tau_{\theta'}$ to 0.7. A decrease of $\tau_{\theta'}$ will include smoother staircases, whereas a high value of $\tau_{\theta'}$ extracts only staircases with 90 degree feature edges. Since the type of staircases should be almost homogeneous within one surface model, the user can adjust the threshold $\tau_{\theta'}$ easily.

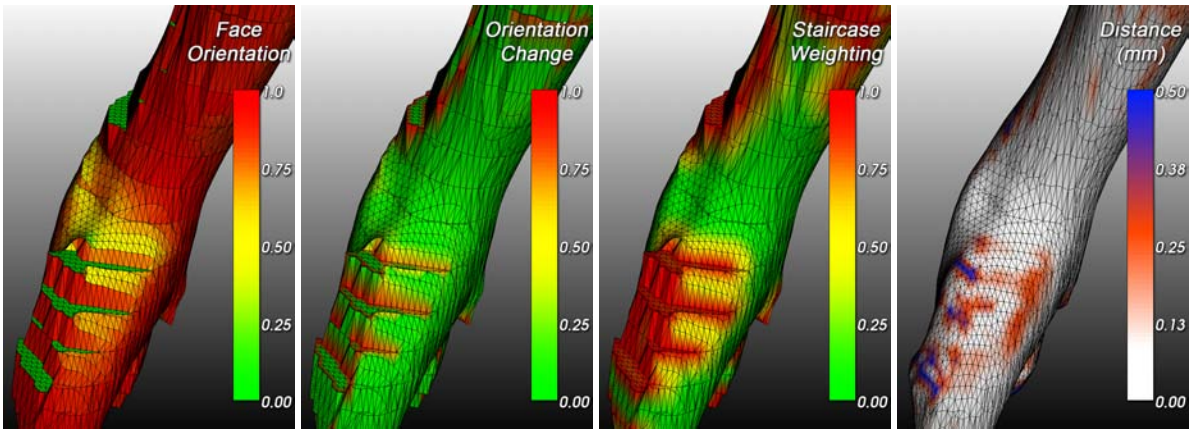

(a) (b) (c) (d)

Figure 4: The single steps of the context-aware smoothing procedure for a part of the geometric model of an arteria carotis: (a) Colored by orientation of the faces in relation to the slice orientation (z-axis). (b) Coloring of the vertices where the orientation of incident faces changes. (c) Vertex weighting according to distance to staircase edges. (d) Final smoothing result colored by local minimum Euclidean distance to the initial model.

Based on the identified staircase vertices, we compute the minimum Euclidean distance d_{v_j} for each vertex v_j in the model to the closest staircase vertex. In this process, we need to exclude the special case, that a non-artifact part of the surface passes a staircase corner vertex very close. This would result in misleading smoothing weights for vertices which do not belong to an artifact. To achieve this, we simply test for topological connectivity within a given range $\tau_{\max}$. The resulting weights w_{v_j} are again scaled according to Eq. 2 to [0,1], where values of 1 occur at the staircase vertices and values of 0 occur in distant parts (see Fig. 4(c)). Additional thresholds give a better control of the staircase weighting. Setting $\tau_{\max}$, the user can define, how far the influence of staircase smoothing reaches into the non-artifact areas. Furthermore, a minimum weight (e.g., $\beta_{min} = 0.1$) for each vertex can be applied, to allow for a user-defined smoothing effect in non-artifact areas without the need to apply an additional smoothing step after context-aware smoothing. As another effect of β_{min}, visually disturbing borders between the smoothed staircases and areas without smoothing (e.g., suffering from noise) can be prevented. The previously computed weights are readjusted to the range above the applied minimum value (see Eq. 3).

$$\forall v_j \in V: \quad w_{v_j} = \begin{cases} \left(1 - \frac{d_{v_j}}{\max(D)}\right) & \text{if } d_{v_j} \leq \tau_{\max}, \\ 0 & \text{if } d_{v_j} > \tau_{\max}. \end{cases} \tag{2}$$

$$w'_{v_j} = w_{v_j} \cdot (1 - \beta_{\min}) + \beta_{\min} \tag{3}$$

$\tau_{\max}$ - max. distance threshold
$\beta_{\min}$ - min. weighting offset
$d_{v_j} \in D; D$ - set of min. Euclidean distances of the vertices V to V'
$V' \in V; V'$ - the extracted staircase vertices
w_{v_j}, w'_{v_j} - distance-related weights for each vertex v_j

3.2.3. Application

After the previous steps, each vertex holds information on the distance to the closest vertex belonging to a staircase corner. These values can be used as weights during the smoothing process to enable an adaptive artifact correction.
Smoothing filters, in general, compute the new position of each vertex by moving it along a displacement vector determined from the original position and the weighted average of the locations of the neighboring vertices (see Eq. 4). This displacement vector can be modified by staircase artifact weighting. Thus, vertices with a weighting value of one are moved according to the applied smoothing algorithm, whereas vertices with a zero weight keep their initial position.

$$\forall v_j \in V: \quad v'_j = v_j + \tfrac{\lambda}{m} \textstyle\sum_{k=1}^{m} (u_k - v_j) \tag{4}$$

$v_j, u_k \in V, \forall u_k \in U^1_{v_j}, m = \left|U^1_{v_j}\right|$
$U^1_{v_j}$ - 1st order neighbors of vertex v_j
λ - uniform smoothing factor

To make the smoothing process adaptive with respect to specific artifacts, we simply need to replace the weighting factor λ by $\lambda' = \lambda \cdot w'_{v_j}$ (see Fig. 4(d) for a sample result). The modification of the smoothing factor, shown above for the Laplace filter, equals to the application of d'_{v_j} to the final displacement vector. Thus, the previously described modification can be applied to any smoothing algorithm. More specific algorithms, such as Laplace+*HC* or Taubin's $\lambda|\mu$, can be employed with their default parameters for smoothing and back correction as usual. The staircase weighting applies only to the final displacement vector resulting from the specific smoothing method with its individual parameters.

3.3. Detection of Caps

The described approach for context-aware smoothing of surface meshes identifies staircase artifacts which are related to the

image stack orientation. During segmentation and model generation, different operations (manual clipping, volume-of-interest bounding box) may yield caps. For consistently handling these flat regions (include/exclude during smoothing), we present a further extension of the adaptive smoothing approach, which allows to detect arbitrarily oriented caps.

First, we identify flat areas by extracting all faces where all

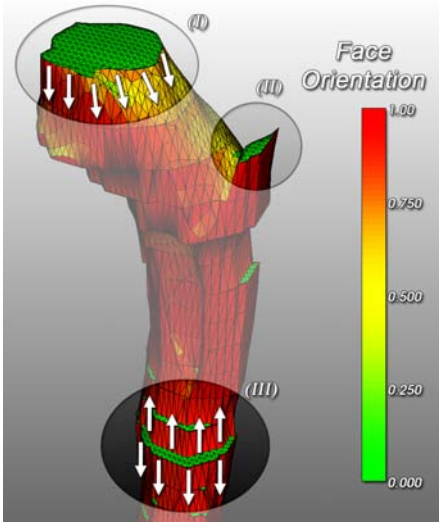

Figure 5: Differentiation between staircases and caps: The latter are characterized by a consistent face direction at the outer cap vertices (I), whereas the direction changes along the vertices of staircases (III). Label (II) highlights a cap-like staircase artifact.

vertices exhibit low maximum normal angles (≤ 5 degree). The result of this operation is a set of separated flat regions (usually all staircases and other low curvature areas), which are cap candidates.

We noticed small artifacts from reconstruction (see Fig. 6, label (III); Fig. 5, label (II)) caused by inhomogeneities in the image data and resulted in small, cap-like structures. However, looking at their size, these structures, as well as scattered single triangles meeting the first low curvature criterion, can be neglected as potential caps using a region size threshold (e.g., 10 faces minimum size). Thus, all small regions will still be subject to smoothing, whereas the larger ones will be examined further. The remaining areas are used as seeds for local region growing. Thus, for each triangle, we iteratively look for neighboring cells whose orientation differs only slightly from the current one. This expands the initially identified areas until feature edges are found.

Our basic assumption for the differentiation between caps and staircases is, that the direction of the surface at the outer cap/staircase vertices (≡ vertices with a high curvature) should be constant for caps (thus pointing consistently along or contrary to the local cap orientation vector; see Fig 5, label (I)). In contrast, for staircases, the direction of the surface at the staircase vertices will change at least twice: from positive to negative and vice versa (see Fig. 5, label (III)). Algorithm 3.1 indicates this differentiation. In each remaining region, we examine the vertices that have been identified as outer staircase vertices. For these vertices, we determine the maximum distance to the first order neighborhood vertices along the specific average cap normal (averaged of all faces belonging to the potential cap). Thus, we consider only those neighboring vertices for comparison, which do not belong to the previously identified cap candidate region. The maximum distance vertex is only needed to determine the direction of the surface: a positive sign means, that the surface continues along the specific cap normal, whereas a negative sign indicates that the surface continues contrary to the orientation vector. Counting the direction changes for each candidate region, we can clearly distinguish between caps and staircases. Finally, regions, where only one direction has been detected at the outer staircase vertices, can be regarded as caps, whereas all other regions with higher values are staircases. As a result, the smoothing weights for the vertices belonging to detected caps are set to zero (see Fig. 6(b), label (I) and (II)). A subsequent smoothing procedure will exclude these vertices to preserve accuracy, whereas staircase areas are reduced (see Fig. 6(c), label (III)).

Algorithm 3.1: CapDetection(*Faces*)

```
// Flat areas: set of separated low curvature areas
FlatAreas ← Faces.getFlatAreas()
CapCandidates ← FlatAreas.labelConnectedComponents()
for each Cap ∈ CapCandidates
do {
    Vertices ← Cap.getBorderVertices()
    DirectionChange ← false
    for i ← 0 to Vertices.getSize()
    {
        // getDistance() returns the signed maximum distance
        // to the vertex neighbors along the orientation vector
        if (i = 0)
          then {Orientation ← sgn(v.getDistance())
          else if (Orientation ≠ sgn(v.getDistance()))
          then {DirectionChange ← true
                break
    if (DirectionChange = true )
      then Cap.delete()
```

4. Results

Context-aware mesh smoothing is usually applied within a pipeline, which may have introduced several inaccuracies (e.g., image noise, inhomogeneities, segmentation errors). Thus, the goal of context-aware smoothing is to strictly avoid additional errors in non-artifact areas and simultaneously make obviously erroneous areas (staircase artifacts) look more plausible. In the following sections, we describe data and the workflow we used for evaluation as well as the related results. However, specific results for the usage of our methods in relation to CFD are shown in Section 5.

4.1. Context-Aware Smoothing

The general suitability of adaptive staircase-aware smoothing has been shown in [5]. To emphasize the benefit of the method, we repeated the evaluation for phantom data and for strongly

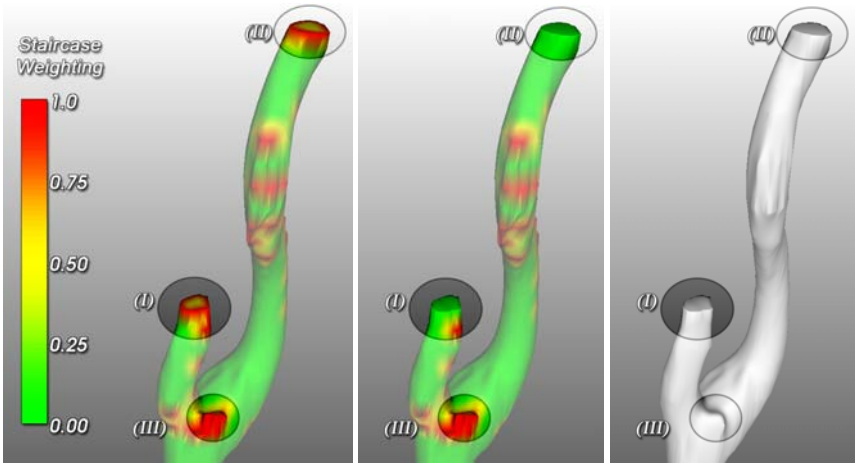

(a) Identified Staircases (b) + Cap Detection (c) After Smoothing

Figure 6: Application of cap detection for a model of the arteria carotis: (a) staircase-like structures are highlighted in red; (b) caps are excluded from staircase weighting; (c) result of context-aware Laplacian smoothing with cap detection. Labels (I) and (II) are caps, whereas (III) is cap-like staircase structure.

anisotropic datasets with more accurate reference models obtained from resampled image data.

4.1.1. Data

We employed two additional structures (vena jugularis, sternocleidomastoid muscle) from CT neck data (voxel size is 0.351×0.351×3.956 mm for both structures). The selected structures contain non-artifact areas as well as parts suffering from staircase artifacts.

The surface meshes have been extracted using a typical workflow. Thus, they have been segmented semi-automatically by medical experts and the resulting binary masks have been dilated (kernel: 3×3×3 voxel). Afterwards, this contour information has been used to mask the intensity data. This allows to account for image inhomogeneities and neighboring structures with similar intensity values. The masked intensity has been used for model generation via MC algorithm. This still results in staircase artifacts, which tend to be large because of the strongly anisotropic voxel dimensions. For better evaluation of distance changes during mesh smoothing, we resampled the masked intensity data to isotropic voxel dimensions (0.351×0.351×0.351 mm) using cubic B-spline interpolation. The default MC mesh (obtained from the anisotropic image data) and the high resolution MC mesh (from resampled data) serve both as reference models for evaluation of distance, volume, and curvature changes.

Furthermore, we employed phantom data to evaluate context-aware smoothing in a context, where the ground truth is known. We built image data containing a sphere, where we deleted parts of the sphere structure in the image data in order to induce staircases (see Fig. 8(b)). The image data has a resolution of 128×128×43 voxels. We selected anisotropic voxel dimensions of 1×1×3 mm to keep the data processing workflow similar to the pipeline used for medical data. Afterwards, we applied Gaussian smoothing to the image data, to allow for the reconstruction of a smooth sphere surface model using MC. As for the previous structures, we resampled the data to isotropic voxel dimensions (0.3×0.3×0.3 mm) to achieve an accurate high resolution surface model as reference. For all structures, we compared context-aware to uniform smoothing approaches:

- Laplacian smoothing (with and without node position constraint (NPC)),
- Laplace+HC,
- Taubin's $\lambda|\mu$.
- Mean Curvature Flow (Laplace with cotangential weights)

For Laplacian smoothing with NPC, we defined cubical voxel cells with the original voxel dimensions for each vertex, whereas the displacement of the vertices during smoothing is restricted to these cells. Since standard Laplacian smoothing may yield strong tangential shifts, we employed the Mean Curvature Flow method, which includes cotangent weights. Context-aware smoothing has been applied to all of these smoothing methods to allow for a direct comparison. For staircase identification, $\tau_{\theta'}$ has been set to 0.7 and $\tau_{\max}$ to 3mm. In non-artifact areas, no smoothing was carried out ($\beta_{min} = 0$) . For the vessel, cap detection has also been applied. According to the analysis in [5], we used 20 iterations and λ=0.5 for the vessel data. For the muscle data, λ has been set to 1, to account for the large staircases. The parameters allow for a sufficient reduction of staircase artifacts for all methods. According to Bade et al. [31], the additional parameters of the Laplace+HC filter have been set to $\alpha = 0$ and $\beta = 0.5$. For Taubin's $\lambda|\mu$ filter, μ equals 0.52 for the vessel data and 1.02 for the muscle data.

The resulting surface models have been compared regarding smoothness, shape and volume preservation. For smoothness, we employed the maximum angle between the vertex normal and the normals of all incident faces, which is less sensitive for degenerated parts of the model than default curvature measures [5]. Volume preservation is analyzed to demonstrate the global error introduced by each mesh smoothing method. The preservation of shape is evaluated with two measures:

- the Hausdorff distance, which is determined between the

Model	Hausdorff Distance to HighRes Model (mm)		ØMin. Euclidean Distance to HighRes Model (mm)		Volume Change (%)		ØNormal Curvature (degree)	
	Uniform	CA	Uniform	CA	Uniform	CA	Uniform	CA
HighRes MC	0		0		0.00		13.55	
Default MC	3.14		0.20		-1.05		26.03	
Laplace	5.17	4.09	0.29	0.22	-7.05	-4.57	6.46	9.72
Laplace+*HC*	3.08	3.08	0.18	0.18	-1.71	-1.56	12.68	16.15
Laplace with NPC	2.94	2.95	0.23	0.21	-4.44	-3.68	11.04	11.59
Taubin's $\lambda\|\mu$	3.15	3.08	0.18	0.18	-1.69	-1.59	12.14	18.00
Mean Curvature Flow	4.43	3.45	0.23	0.20	-4.91	-3.45	8.07	12.00

Table 1: Results for the comparison of smoothing methods for the data of the sternocleidomastoid muscle: Each smoothing method has been combined with context-aware smoothing (CA). NPC stands for "node position constraint". The ØNormal Curvature is slightly higher for the CA approaches, since major parts the the original surface remain unchanged.

smoothed and the high resolution surface and
- the average minimum Euclidean distance between the smoothed and the high resolution reference model.

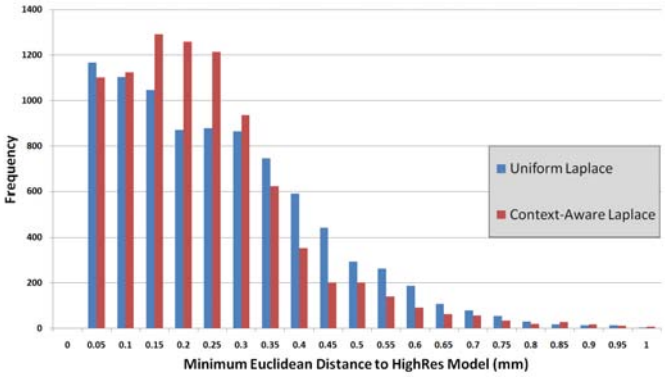

Figure 7: Changes of minimum Euclidean distance of uniform and context-aware Laplacian smoothing of the model of the vena jugularis. Context-aware smoothing reduces the number of larger distance changes.

4.1.2. Evaluation

The comparison of the employed methods reveals, that context-awareness could successfully restrict the smoothing process to the artifact areas. In combination with context-aware smoothing, the accuracy of all involved uniform smoothing methods could be increased.

As expected, standard Laplacian smoothing yielded strongest volume shrinkage for both anatomical structures (SCM:-7.05%; v. jugularis: -3.53%; see Tab. 1 and 2) as well as for the phantom data (-4.02%, see Tab. 3). This error could clearly be decreased by context-aware smoothing (SCM:-4.57%; v. jugularis: +1.08%; phantom: -0.48). The volume changes for the more volume- and feature-preserving methods, such as Laplace+*HC*, Laplace with NPC, Taubin's $\lambda|\mu$ filter, and Mean Curvature Flow, are smaller. We could, however, generally improve the individual results. For the vessel model (see Tab. 2), most methods yield a volume increase which results from a large concavely shaped area. The sphere phantom data shows the strongest differences between the uniform and context-aware methods.

The error in terms of distance changes (Hausdorff distance, average mininum Euclidean distance) could also be reduced by context-aware smoothing for the Laplace, Taubin's $\lambda|\mu$ filter, and Mean Curvature Flow for all tested models. The combination with Laplace+*HC* as well as Laplace with NPC did not yield relevant changes for the Hausdorff distance. We have noticed slight improvements for the average minimum Euclidean distance to the high resolution model for Laplace with and without NPC. Figure 7 shows for Laplacian smoothing, that context-aware smoothing (red bars) is able to decrease the number of large distance changes compared to the uniform method (blue bars). These differences are obviously smaller for more restrictive smoothing methods (e.g., Laplace+*HC*, LaplaceNPC, Taubin's $\lambda|\mu$ filter).

The smoothness in terms of average normal curvature is always slightly higher for the context-aware approaches. This is obvious, since major parts of the surface models have been smoothed less. Since the high resolution mesh is smoother by definition (due to the interpolated image data), we included the default MC mesh as reference for smoothness. Context-aware smoothing could reduce the curvature in all cases, but represents a tradeoff between accuracy and smoothness. Thus, the uniform smoothing methods yielded smoother surfaces. The average normal curvature for context-aware smoothing can be reduced by setting β_{min} to 0.1 or 0.2 for a restrained smoothing effect in non-artifact areas.

According to Tab. 1, the sequence of the five methods in terms of accuracy (especially Hausdorff distance) remains the same for the uniform and the context-aware approach. For the vessel data (see Tag. 2), the sequence is modified. Context-aware smoothing improves the accuracy of uniform Laplacian smoothing to be similar and even slightly better than the more restrictive methods.

The results have shown, that context-aware smoothing could at least keep the accuracy of the initial models and, in almost all cases, preserve the volume better then the employed uniform smoothing methods. Furthermore, it does not introduce essential additional effort to the model generation pipeline. Identification and weighting of staircases took less then one second for all employed surface models. The default parameters did not have to be adjusted. The parameters yield, however,

Model	Hausdorff Distance to HighRes Model (mm)		ØMin. Euclidean Distance to HighRes Model (mm)		Volume Change (%)		ØNormal Curvature (degree)	
	Uniform	CA	Uniform	CA	Uniform	CA	Uniform	CA
HighRes MC	0		0		0.00		12.83	
Default MC	1.40		0.22		+3.07		25.74	
Laplace	2.63	1.40	0.24	0.21	-3.53	+1.08	7.31	12.12
Laplace+*HC*	1.60	1.54	0.22	0.22	+3.68	+3.48	13.08	17.64
Laplace with NPC	1.80	1.40	0.23	0.21	-1.40	+1.87	10.38	13.18
Taubin's $\lambda\|\mu$	1.50	1.45	0.22	0.22	+3.78	+3.29	15.01	22.26
Mean Curvature Flow	1.80	1.44	0.21	0.20	-0.22	+1.62	8.92	13.05

Table 2: Results for the comparison of smoothing methods for the data of the vena jugularis: Each smoothing method has been combined with context-aware smoothing (CA). NPC stands for "node position constraint".

Model	Hausdorff Distance to HighRes Model (mm)		ØMin. Euclidean Distance to HighRes Model (mm)		Volume Change (%)		ØNormal Curvature (degree)	
	Uniform	CA	Uniform	CA	Uniform	CA	Uniform	CA
HighRes MC	0		0		0.00		0.44	
Default MC	2.73		0.04		-0.01		1.72	
Laplace	1.96	1.51	0.57	0.06	-4.02	-0.48	1.37	1.49
Laplace+*HC*	2.08	2.09	0.03	0.03	-0.02	0.00	1.61	1.67
Laplace with NPC	1.51	1.51	0.42	0.04	-2.91	-0.04	2.45	1.47
Taubin's $\lambda\|\mu$	2.20	2.21	0.03	0.03	-0.01	0.00	1.70	1.71
Mean Curvature Flow	1.64	1.61	0.29	0.04	-2.17	-0.02	2.46	1.475

Table 3: Results for the comparison of smoothing methods for the sphere phantom data: Each smoothing method has been combined with context-aware smoothing (CA). NPC stands for "node position constraint".

stable results for small changes. Thus, a time-consuming parameter tuning is not necessary.

4.2. Estimation of the Image Stack Orientation

We applied orientation estimation to three differently shaped MC surface models of the arteria carotis, the sternocleidomastoid muscle (SCM), and the liver which have all been extracted with the workflow described in Section 4.1.1. We rotated the initial models around the x-axis and the y-axis separately up to 90 degree in 30 degree steps. Finally, we compared the accuracy of the estimated orientation vector to the one known by the applied rotation. The radius r has been set to 0.1 for all employed datasets. Even small changes (e.g., 0.05 or 0.2) did not yield significant changes.

The results of the experiments are shown in Table 4. The average estimation error (deviation from the known orientation vector) of all structures is 0.444 degree. The individual structures containing large staircase areas, but also non-artifact parts, showed slight differences: 0.830 (arteria carotis), 0.481 (SCM), and 0.021 (liver) degree.

The accuracy of the orientation estimation depends strongly on the presence and size of flat areas related to the image stack orientation, as contained in staircases and caps. Thus, for models with very few staircase artifacts, our approach might be less accurate. To evaluate this aspect, we employed phantom image data of a sphere, where we cut out parts of the topmost image data slice with increasing size to generate a staircase-like flat area, which our approach requires to estimate the image stack orientation. We used five steps: 1/16th, 1/8th, 1/4th, 1/2, and a complete removal of the topmost sphere slice (see Fig. 8(a)). All of these cuts have been applied in the axial images, thus the target orientation, that our approach should detect is a vector along the z-axis, e.g., (0,0,1).

Subsequently, we measured the size of the resulting flat areas in terms of the percentage to each surface model (see Tab. 5). For each of the models, the orientation has been estimated. Less than 0.40 % of the faces in these phantom models were sufficient to detect the image stack orientation with an acceptable accuracy. The estimation failed for the model with only

Rotation Axis	Rotation Angle	Arteria Carotis	SCM	Liver
	0	0.830	0.479	0.000
X	30	0.828	0.484	0.046
	60	0.830	0.483	0.026
	90	0.830	0.479	0.000
Y	30	0.830	0.480	0.032
	60	0.831	0.482	0.034
	90	0.830	0.479	0.000
Average	-	0.830	0.481	0.021

Table 4: Results for the estimation of the image stack orientation applied to three differently shaped structures: For the vessel (arteria carotis), a muscle (sternocleidomastoid muscle, SCM) and the liver, the deviation angles towards the known orientation vector are presented (in degree).

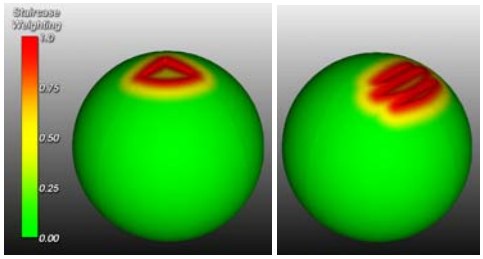

(a) (b)

Figure 8: Samples of the phantom data employed for evaluation of orientation estimation and staircase identification: (a) has been derived from phantom image data, where a quarter of topmost slice of the sphere has been removed. (b) is an example for manually introduced staircases to evaluate accuracy.

0.17% of the faces being oriented along the image stack orientation. For the latter, not only faces orthogonal to the orientation vector have been generated. Especially at the borders between the original sphere surface and the cut parts, a lot of diagonal faces emerged. Thus, an accurate detection of the image stack orientation was not possible.

Amount Removed	% Flat Faces	Deviation Angle
1/16	0.17	10.284
1/8	0.40	1.629
1/4	0.78	1.621
1/2	1.63	1.174
Complete Slice	3.09	0.000

Table 5: Results for the comparison of phantom sphere data with differently sized staircase-like artifacts: In the topmost sphere slice, differently sized parts have been removed. The percentage of flat faces is the number of faces oriented along the known image stack orientation in relation to the total number of faces in the model.

4.3. Detection of Caps

To demonstrate the capabilities of the cap detection method, we employed phantom data in terms of a cylinder merged with a cuboid. Thus, the resulting structure contains perfect caps due to the cylinder and staircases due to the cuboid (see Fig. 9(a) and 9(b)). The surface model has again been generated via MC from artificially created image data. We extract the surface model from image data instead of directly generating the mesh in order to keep the mesh properties close to the pipeline used for medical structures. Subsequently, we applied uniform Laplacian mesh smoothing to the phantom surface model to generate variations with increasing smoothness and thus less feature edges. We applied up to 50 iterations with $\lambda = 0.5$. With that procedure, we did not aim at quantitative evaluation of (context-aware) smoothing. We evaluated, if the cap detection method is still able to differentiate between the cap-like parts of the model and the staircases. Sample results are shown in Figure 9. Figure 9(c) (50 iterations) demonstrates, that the caps and staircases have been identified correctly and could be excluded from the list of potential staircases (see Fig. 9(d)).
The detection of caps and further exclusion from staircase weighting requires, that the cap has initially been detected as staircase. Since the feature edges at the caps and staircases exhibit very low curvature, we decreased $\tau_{\theta'}$ to 0.2 to detect these parts as staircases. This low value for $\tau_{\theta'}$, however, has never been required for clinical data where potential caps exhibit sharper feature edges. Finally, for all created phantom models, the caps could be detected.

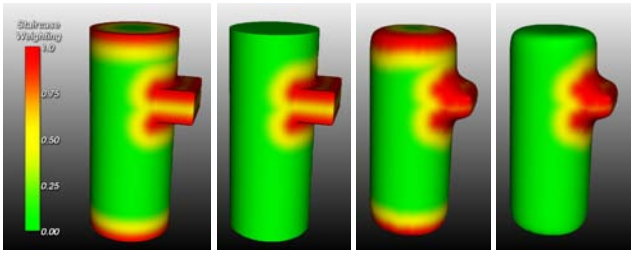

(a) (b) (c) (d)

Figure 9: Phantom data used to evaluate cap detection for differently smoothed caps: (a) and (b) depict the initial surface model after default staircase weighting (a) and with cap detection enabled (b). The models in (c) and (d) show the same procedure, but for smoothed models (Laplace, 50 iterations, $\lambda = 0.5$) without sharp feature edges.

5. Application to Computational Fluid Dynamics

An application, where accuracy and smoothness are especially relevant, is the patient-specific simulation of blood flow, e.g., in cerebral aneurysms. We selected this application, since the simulation results in terms of flow velocity and wall shear stress may strongly depend on details of the patient-specific geometry and corresponding mesh smoothing operations. Thus, the careful reduction of segmentation artifacts, such as merged vascular branches due to image inhomgeneities, is often a tedious, time-consuming manual procedure.
Applying context-aware smoothing to models for CFD, we shall investigate two questions:

(I) Can context-aware smoothing reduce the effort for manual correction of local artifacts?
(II) What are the differences between the employed smoothing methods with respect to the blood flow behaviour?

In this section, we describe the employed data and the specific model generation pipeline. Finally, we discuss the results of the blood flow simulation for different smoothing methods with and without context-awareness.

5.1. Data and Workflow

The steps of our CFD model generation pipeline are shown in Fig. 10. Clinical or phantom image data for blood flow simulation can be derived from different modalities (e.g., magnetic resonance angiography (MRA), computed tomography angiography (CTA), rotation angiography, time-of-flight MR angiography). For evaluation of context-aware smoothing, we employed CTA data of a phantom aneurysm model (voxel size is 0.4×0.4×0.4 mm). Due to the high contrast in the angiography

data, vascular structures can be delineated easily by an intensity threshold. Afterwards, we apply a connected component analysis to extract the aneurysm and its parent vessel (inlets, outlets) from background noise. Manual effort has been necessary to define an ROI around the aneurysm to exclude bone structures and distant vessels. The resulting segmentation information has been used to mask the initial intensity data. As in many datasets, image inhomogeneities yield wrong contour information. In the employed phantom dataset, beam hardening artifacts at the two aneurysm outlets lead to blending effects in the subsequent MC model generation step. Additional effort was necessary to correct the segmentation mask by manually drawing contours in the image slices of the affected vessel regions. Unfortunately, this procedure leads to staircase-like artifacts in the surface model. Thus, a final smoothing of the surface mesh is necessary to remove surface noise, but especially staircase artifacts from image segmentation. A typical solution is the manual correction of local artifacts, e.g., employing tools, such as *Sculptris*[1] for dynamic mesh tesselation, surface modeling and smoothing. Such a manual procedure is, however, time-consuming and error-prone. In contrast, automatic mesh smoothing might not guarantee the required accuracy and smoothness simultaneously. Thus, adaptive mesh smoothing might allow for accurate and smooth surface models applicable to CFD. As a result of mesh smoothing, the homogeneity of the triangle size and quality is usually slightly improved. After the smoothing step, the inlets and outlets are cut orthogonal to the local vessel centerline to define valid inflow and outflow regions for the CFD simulation. Finally, we optimize the reconstructed surface mesh with respect to the mesh quality by employing an advancing front remeshing algorithm [44]. The resulting mesh is subsequently used for volume grid generation, which is used for the CFD simulation.

The numerical computations are performed in parallel using up to six computing cores applying the commercial CFD solver ANSYS Fluent 12. Blood rheology is represented using a Newtonian description with constant density and viscosity, where the blood density is chosen as 1000 kg/m^3 and the dynamic viscosity as $4 \cdot 10^{-3} Pa \cdot s$. In the present case, a steady flow condition is finally retained with an inlet flow rate of 1.2 cm^3/s at the inlet. All vascular walls are assumed to be rigid, as in most published studies, since real wall material properties are unknown. A standard, no-slip boundary condition is employed at all contact points with surfaces. At the outlets, traction-free boundary conditions are applied.

To evaluate the influence of context-aware mesh smoothing, we employed Laplace and Laplace+*HC* filtering to the initial MC mesh. Each method has also been combined with context-aware smoothing. Taubin's $\lambda|\mu$ smoothing and Laplace with NPC have been omitted here, since they usually yield intermediate smoothing results compared to Laplace, which provokes strongest errors, and Laplace+*HC*, which is very restrictive. Furthermore, we employed a manually smoothed and adjusted model as reference model. An overview about the models with their quantitative differences compared to the manually smoothed model is given in Table 6. We defined this surface as reference model because of the best trade-off between adaptive smoothness and volume preservation to the original MC model. We assume it fits best to the original vessel surface and the resulting CFD results are more valid in contrast to the other models. Note, we compare the CFD results under the given boundary conditions. Predictions about the validation of simulated blood flow to the real flow behavior is still a research task [45]. The numerical results of the CFD simulation, namely velocity and wall-shear-stress (WSS) are listed in Tab. 6.

[1] www.sculptris.com

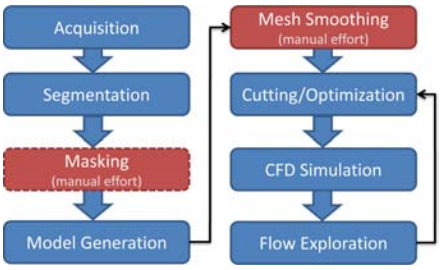

Figure 10: Overview about the CFD data flow pipeline from image aquisition to a meaningful CFD simulation model. In some cases a masking step with manual effort is necessary to resolve blending artifacts which leads to staircase-like artifacts. Hence, an adaptive smoothing approach is necessary to resolve these artifacts.

5.1.1. Results and Discussion

In the upper left corner of Figure 11, the reference model of the reconstructed aneurysm surface with its inlet and two outlets is shown. Blood flow and velocity magnitude is visualized with color-coded streamlines. An ROI around the staircase-like artifact (existent in the original MC model) is marked and enlarged for each surface model next to the aneurysm (first row). Additionally, the corresponding WSS (second row) and velocity magnitude (third row) of that ROI are presented. Laplacian smoothing caused the strongest volume change (-18.69%) resulting in an increased velocity magnitude and WSS because of the small vessel diameters. Context-aware smoothing could reduce volume shrinkage to -4.53% which comes along with a strong reduction of WSS. Comparing uniform and context-aware Laplacian smoothing to our manually smoothed reference model shows still strong differences. Uniform Laplace+*HC* filtering could again reduce volume shrinkage and distance changes resulting in less errors for velocity and WSS. Adding context-awareness to Laplace+*HC* filtering could improve the results and get closer the reference model.

The results demonstrate clearly, that mesh smoothing influences the results of blood flow simulations strongly. Context-aware smoothing could clearly improve the results of the employed uniform smoothing methods. Laplace+*HC* smoothing combined with context-awareness achieved the smallest error compared to manual smoothing. Keeping in mind, that the manually smoothed model might also not perfectly describe the real flow behaviour, context-aware Laplace+*HC* smoothing might be a promising alternative to the time-consuming manual artifact correction procedure.

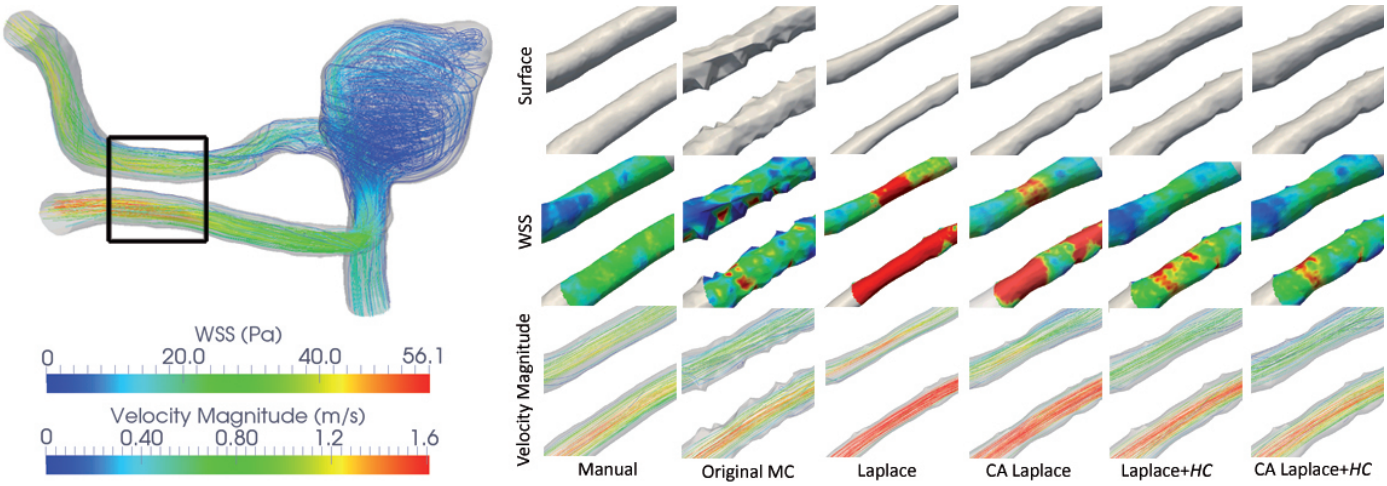

Figure 11: Comparison of the CFD results for the employed smoothing methods. The manually smoothed reference model is shown in the upper left corner with color-coded streamlines. A region of interest is defined (black rectangle) around the artifact area and is enlarged for the six models on the right side. The maximum of the color scales is related to the reference model.

Model	Hausdorff Dist. (mm)	ØMin. Euclid. Distance (mm)	Volume Change(%)	ØNormal Curv. (degree)	Max. Vel. (m/s)	Max. WSS ROI (Pa)	Difference Vel. / WSS
Manual	0	0	0	6.224	1.611	56.135	0 / 0
Original MC	0.497	0.083	-1.05	6.528	1.696	142.824	0.085 / 86.689
Laplace	0.649	0.253	-18.69	6.239	4.281	345.573	2.670 / 289.438
CA Laplace	0.511	0.085	-4.53	6.372	2.591	164.901	0.980 / 108.766
Laplace+*HC*	0.499	0.078	-3.0	6.382	1.941	103.923	0.330 / 47.788
CA Laplace+*HC*	0.401	0.07	-1.49	6.32	1.717	94.037	0.106 / 37.902

Table 6: Overview of the six smoothing variations of the aneurysm model on which a CFD simulation is performed. In all cases our context-aware smoothing results in a more volume preserved smoothing compared to standard Laplace or Laplace+*HC*. Distance differences and volume change are related to the manual smoothed model.

6. Conclusion

To reduce staircase-artifacts in medical surface models, we have presented context-aware mesh smoothing, which is an extended approach for the improvement of the accuracy of common uniform mesh smoothing algorithms. Thus, artifacts can be adaptively smoothed, whereas accuracy and features are preserved in non-artifact areas of the surface model. This is especially relevant for surgical planning, where pathological structures need to be evaluated and quantified. We enable the automatic estimation of model orientation and detect cap-like structures to be preserved during the smoothing procedure.
The estimation of model orientation is based on clustering of face normals. The results have proven, that the presented approach is able to reliably detect the correct model orientation, if a relevant number and size of staircase artifacts is available. We assume, however, that we can further improve the results to allow for a correct orientation detection with less artifacts by a more detailed analysis of the clusters formed by similar normals. Since we only require an arbitrary vector along the model orientation axis (e.g., z-axis), we might combine the information of inverse normal clusters. Thus, the clusters for vectors, such as $\vec{v_1}(0,0,1)$ and $\vec{v_2}(0,0,-1)$ would be merged during analysis resulting in higher cluster density.
Evaluating the results for the detection of caps has also shown the reliability of the method. To generalize it further, we need to extend it to detect caps, which are not related to the image stack orientation as, e.g., in aneurysm models for flow simulation, where the model is usually edited to define correct inlets and outlets orthogonal to the vessel centerline. This might be achieved by analyzing homogeneous areas if the model with respect to the relative orientation θ_{f_i} and curvature. Furthermore, we examined the accuracy of context-aware smoothing, which could confirm the results of our previous paper [5]. Comparing the distance and volume changes to high resolution reference models instead of the default MC models has shown improvements for all employed anatomical structures as well as for phantom data. The changes of Hausdorff distance and average minimum Euclidean distance lie within the submillimeter/subvoxel range. This is, however, related to the size of the artifacts and voxel size. The visual results but also the application of context-aware smoothing to CFD demonstrate, that context-aware smoothing is able to preserve non-artifact areas better then uniform smoothing approaches. For surface models, where only small parts suffer from staircase artifacts, the strongest visual and quantitative gain is achieved.

Acknowledgments: We thank Santhosh Seshadhri (ISUT Magdeburg) for preparing the volume models for CFD simulation. Tobias Moench

is funded by the German Federal Ministry of Education and Research (BMBF) within the ViERforES-II project (no. 01IM10002A).

References

[1] Kobbelt LP, Botsch M, Schwanecke U, Seidel HP. Feature sensitive surface extraction from volume data. In: Proc. of the ACM SIGGRAPH Conference on Computer Graphics. 2001, p. 57–66.

[2] Desbrun M, Meyer M, Schröder P, Barr AH. Implicit fairing of irregular meshes using diffusion and curvature flow. In: Proc. of the ACM SIGGRAPH Conference on Computer Graphics. 1999, p. 317–24.

[3] Vollmer J, Mencl R, Müller H. Improved laplacian smoothing of noisy surface meshes. Computer Graphics Forum 1999;18(3):131–8.

[4] Tasdizen T, Whitaker R. Anisotropic diffusion of surface normals for feature preserving surface reconstruction. In: Proc. of 3-D Imaging and Modeling. 2003, p. 353–60.

[5] Mönch T, Adler S, Preim B. Staircase-aware smoothing of medical surface meshes. In: Eurographics Workshop on Visual Computing for Biology and Medicine (VCBM). 2010, p. 83–90.

[6] Hahn H, Preim B, Selle D, Peitgen HO. Visualization and Interaction Techniques for the Exploration of Vascular Structures. In: Proc. of IEEE Visualization. 2001, p. 395–402.

[7] Radtke A, Sotiropoulos GC, Molmenti EP, Schroeder T, Peitgen HO, Frilling A, et al. Computer-assisted surgery planning for complex liver resections: when is it helpful? a single-center experience over an 8-year period. Ann Surg 2010;252(5):876–83.

[8] Zidowitz S, Hansen C, Schlichting S, Kleemann M, Peitgen HO. Software assistance for intra-operative guidance in liver surgery. In: World Congress on Medical Physics and Biomedical Engineering; vol. 25/6. Springer Berlin Heidelberg; 2009, p. 205–8.

[9] Schenk A, Zidowitz S, Bourquain H, Hindennach M, Hansen C, Hahn HK, et al. Clinical relevance of model based computer-assisted diagnosis and therapy. In: Proc. of SPIE Medical Imaging; vol. 6915. 2008,.

[10] Fischer L, Schoebinger M, Neumann JO, Müller S, Meinzer HP, Büchler M, et al. Does preoperative analysis of intrahepatic venous anastomoses improve the surgeon's intraoperative decision making? pilot data from a case report. Patient Safety in Surgery 2008;2(1):19–23.

[11] Radtke A, Nadalin S, Sotiropoulos GC, Molmenti EP, Schroeder T, Valentin-Gamazo C, et al. Computer-assisted operative planning in adult living donor liver transplantation: a new way to resolve the dilemma of the middle hepatic vein. World J Surg 2007;31(1):175–85.

[12] Ellis RE, Tso CY, Rudan JF, Harrison MM. A surgical planning and guidance system for high tibial osteotomy. Computer Aided Surgery 1999;4(5):264–74.

[13] Hertel I, Strauß G, Schulz T, Dornheim J, Cordes J, Krüger A, et al. 3-D Visualisation of CT-data for Surgical Planning in Trachea Resection: Proof of Concept. In: Proc. of Computer-Assisted Radiology and Surgery (CARS). Springer; 2006, p. 312–4.

[14] Mönch T, Neugebauer M, Hahn P, Preim B. Generation of Smooth and Accurate Surface Models for Surgical Planning and Simulation. In: Proc. of SPIE Medical Imaging. 2010,.

[15] Neubauer A, Forster MT, Wegenkittl R, Mroz L, Bühler K. Efficient display of background objects for virtual endoscopy using flexible first-hit ray casting. In: Proc. of Eurographics/IEEE TVCG Symposium on Visualization. 2004, p. 301–310, 352.

[16] Raya S, Udupa J. Shape-based interpolation of multidimensional objects. IEEE Transactions on Medical Imaging 1990;9(3):32–42.

[17] Lorensen WE, Cline HE. Marching cubes: A high resolution 3d surface construction algorithm. In: Proc. of the ACM SIGGRAPH Conference on Computer Graphics. 1987, p. 163–9.

[18] Whitaker RT. Reducing aliasing artifacts in iso-surfaces of binary volumes. In: Proc. of the IEEE symposium on volume visualization. 2000, p. 23–32.

[19] Allamandri F, Cignoni P, Montani C, Scopigno R. Adaptively adjusting marching cubes output to fit a trilinear reconstruction filter. In: Proc. of EG Workshop on Scientific Visualization. 1998, p. 25–34.

[20] Nielson GM. Dual marching cubes. In: Proc. of IEEE Visualization. 2004, p. 489–96.

[21] Gibson SFF. Constrained elastic surface nets: Generating smooth surfaces from binary segmented data. In: Proc. of MICCAI. 1998, p. 888–98.

[22] Bruin PWD, Vos FM, Post FH, Frisken-Gibson SF, Vossepoel AM. Improving triangle mesh quality with surfacenets. In: Proc. of MICCAI. 2000, p. 804–13.

[23] Taubin G. A signal processing approach to fair surface design. In: Proc. of the ACM SIGGRAPH Conference on Computer Graphics. 1995, p. 351–8.

[24] Hornung A, Kobbelt L. Robust reconstruction of watertight 3d models from non-uniformly sampled point clouds without normal information. In: Proc. of the 4th Eurographics symposium on Geometry processing. SGP '06; 2006, p. 41–50.

[25] Jones TR, Durand F, Desbrun M. Non-iterative, feature-preserving mesh smoothing. ACM Trans Graph 2003;22(3):943–9.

[26] Bobenko AI, Schröder P. Discrete willmore flow. In: ACM SIGGRAPH 2005 Courses. SIGGRAPH '05; 2005, p. 101–10.

[27] Lempitsky V. Surface extraction from binary volumes with higher-order smoothness. In: Proc. of the IEEE Conference on Computer Vision and Pattern Recognition. 2010, p. 1197–204.

[28] Nealen A, Igarashi T, Sorkine O, Alexa M. Laplacian mesh optimization. In: Proc. of the 4th International Conference on Computer Graphics and Interactive Techniques. GRAPHITE '06; ACM; 2006, p. 381–9.

[29] Li Z, Ma L, Jin X, Zheng Z. A new feature-preserving mesh-smoothing algorithm. Vis Comput 2009;25(2):139–48.

[30] Belyaev A, Ohtake Y. A comparison of mesh smoothing methods. In: Proc. of the Israel-Korea BiNational Conference on Geometric Modeling and Computer Graphics. 2003, p. 83–7.

[31] Bade R, Haase J, Preim B. Comparison of fundamental mesh smoothing algorithms for medical surface models. In: Proc. of Simulation und Visualisierung. 2006, p. 289–304.

[32] Bade R, Konrad O, Preim B. Reducing artifacts in surface meshes extracted from binary volumes. Journal of WSCG 2007;15(1-3):67–74.

[33] Huang H, Ascher U. Surface mesh smoothing, regularization, and feature detection. SIAM J Sci Comput 2008;31(1):74–93.

[34] Ohtake Y, Belyaev A, Seidel HP. Mesh smoothing by adaptive and anisotropic gaussian filter applied to mesh normals. In: Proc. of Vision, Modeling and Visualization. 2002, p. 203–10.

[35] Bajaj CL, Xu G. Adaptive fairing of surface meshes by geometric diffusion. In: International Conference on Information Visualisation. 2001, p. 731–7.

[36] Chen CY, Cheng KY. A sharpness dependent filter for mesh smoothing. Computer Aided Geometric Design 2005;22(5):376 –91.

[37] Garland M, Heckbert PS. Surface simplification using quadric error metrics. In: Proceedings of the ACM SIGGRAPH Conference on Computer Graphics. 1997, p. 209–16.

[38] Hoppe H. Progressive Meshes. In: Proc. of the ACM SIGGRAPH Conference on Computer Graphics. 1996, p. 99–108.

[39] Cebral JR, Mut F, Weir J, Putman CM. Association of hemodynamic characteristics and cerebral aneurysm rupture. AJNR Am J Neuroradiol 2011;32(2):264–70.

[40] Cebral JR, Löhner R, Soto O, Choyke PL, Yim PJ. Patient-specific simulation of carotid artery stenting using computational fluid dynamics. In: Proc. of MICCAI. 2001, p. 153–60.

[41] Cebral JR, Castro MA, Appanaboyina S, Putman CM, Millan D, Frangi AF. Efficient pipeline for image-based patient-specific analysis of cerebral aneurysm hemodynamics: technique and sensitivity. IEEE Trans Med Imaging 2005;24(4):457–67.

[42] Augsburger L, Reymond P, Ouared R, Brina O, Rufenacht DA, Stergiopulos N, et al. Influence of segmentation on hemodynamics in cerebral aneurysms. In: Proc. of Conference on Modelling Fluid Flow. 2009, p. 81–7.

[43] Bade R, Schumann C, Seshadhri S, Janiga G, Bölke T, Özlem Krischek , et al. High-quality surface generation for flow simulation in cerebral aneurysms. In: Proc. of Computer- und Roboterassistierte Chirurgie (CURAC). 2007, p. 125–8.

[44] Schöberl J. Netgen - an advancing front 2d/3d-mesh generator based on abstract rules. In: Computing and Visualization in Science; vol. 1. 1997, p. 41–52.

[45] Boussel L, Rayz V, Martin A, Acevedo-Bolton G, Lawton MT, Higashida R, et al. Phase-contrast magnetic resonance imaging measurements in intracranial aneurysms in vivo of flow patterns, velocity fields, and wall shear stress: Comparison with computational fluid dynamics. Magnetic Resonance in Medicine 2009;61(2):409–17.